

Oxygen vacancy self-doping strategy efficiently enhanced Ce^{3+} and chemical-mechanical polishing properties of CeO_2 .

Author: Wenliang Chen^a, Jilin Wang^b, Xin Tang^a, Xiaodong An^a, Wenke Guan^a, Changyu Liu^a, Daijiang Peng^{a*}

^aSchool of Materials Science and Engineering, Guilin University of Technology, Guilin 541004, China

^bGuangxi Key Laboratory of Optical and Electronic Materials and Devices, Collaborative Innovation Center for Exploration of Nonferrous Metal Deposits and Efficient Utilization of Resources, School of Materials Science and Engineering, Guilin University of Technology, Guilin 541004, China

***Corresponding author: E-mail: pdj@glut.edu.cn (Daijiang Peng)**

Abstract

The synergistic effect of photochemical oxidizing activity and frictional chemistry capability of CeO_2 is essential for the development of photocatalytic-assisted chemical mechanical polishing (PCMP) abrasive system. However, the limitations of CeO_2 , including its wide band gap (~ 3.2 eV) and high rate of photogenerated carrier recombination, significantly restrict the enhancement of CeO_2 's photochemical activity. This, in turn, obstructs the broader application of CeO_2 abrasives in post-CMP processes. As a result, this experiment employed the oxidation reaction between H_2O_2 and CeOHCO_3 to generate $\text{Ce}(\text{O}_2)(\text{OH})_2$ intermediates. Furthermore, CeO_2 with a high concentration of oxygen vacancies (labeled as NCeO_2) was successfully synthesized through the thermal decomposition of Ce-O_2^{2-} in a nitrogen environment. The analysis revealed that NCeO_2 exhibited higher concentrations of V_O and Ce^{3+} , as well as enhanced electron-hole separation efficiency and photochemical activity. Additional examination of the electronic structure of CeO_2 using first-principles calculations demonstrated that a high concentration of oxygen vacancies creates intermediate energy states near the Fermi level. This condition reduces the bandgap of CeO_2 , thereby enhancing its photochemical activity. The polishing application demonstrated that the

NCeO₂ abrasive exhibited superior polishing performance, achieving the lowest surface roughness ($R_a = 0.217 \pm 0.007$ nm) and root-mean-square roughness ($RMS = 0.279 \pm 0.01$ nm) compared to commercial abrasives ($R_a = 0.77$ nm, $RMS = 1.41$ nm), reducing R_a and RMS by 71.8 % and 80.1 %, respectively. These results suggest that the oxygen vacancy self-doping strategy effectively enhances the concentrations of Ce³⁺ and oxygen vacancies in CeO₂, thereby improving its photochemical activity. This approach offers a novel concept for the further application of CeO₂ abrasives in PCMP.

Keywords: CeO₂ abrasives, oxygen vacancy, cerium peroxo, density functional theory (DFT), photochemical mechanical polishing (PCMP)

1. Introduction

Silicon dioxide (SiO₂) has undergone extensive research and development for various applications in the semiconductor industry, primarily because of its outstanding physical and chemical properties, including high-temperature resistance, corrosion resistance, and high optical permeability. However, the increasing demand for high-performance semiconductor devices in advanced fields such as information display, aerospace, and renewable energy has resulted in stricter requirements for the flattening of glass substrates. The practical application of SiO₂ remains constrained by surface quality. Cook^[1] proposed a polishing mechanism for SiO₂ substrates utilizing CeO₂ abrasives. In this polishing mechanism, the Ce³⁺ on the CeO₂ surface acts as a strong chemical reaction site, weakening the bond between Si and O on the SiO₂ film. This results in the formation of a Ce-O-Si chemical bond, which enables more efficient surface planarization. The combined effect of mechanical abrasion and chemical reaction can result in the formation of CeO₂ abrasives with a high material removal rate and excellent surface finish. Furthermore, Ce³⁺ has been demonstrated to exert a significant influence on the enhancement of polishing quality.

Presently, CeO₂ is greatly limited for polishing applications due to its inherent deficiencies in hardness and low surface defects (Ce³⁺ and V_o).^[2] In order to enhance the polishing efficacy of CeO₂, photocatalytic-assisted chemical-mechanical polishing (PCMP) has garnered increasing attention in recent years. In PCMP applications, the

abrasive acts as a photocatalyst to be excited under UV radiation, generating oxidized substances ($\cdot\text{OH}$, $\cdot\text{O}^{2-}$, etc.) during the polishing process, promoting the formation of the chemical (or photochemical) reactive layer $\text{Si}(\text{OH})_4$, decreasing the hardness of SiO_2 , and accelerating the removal of the SiO_2 material.^[3] Currently, CeO_2 -based composite abrasives have been further developed for PCMP, with the expectation that CeO_2 will provide photocatalytic oxidation and friction chemical removal capabilities.^[4-8] However, the significant bandgap (~ 3.1 eV) and high rate of electron-hole complexation in CeO_2 negatively affect its photochemical activity, limiting its widespread application in PCMP. Consequently, enhancing the photochemical activity of CeO_2 to improve the polishing effectiveness and performance of CeO_2 -based abrasives has emerged as a vital area of research. A number of methods have been proposed to overcome these drawbacks, such as cationic or anionic doping^[9-14], heterogeneous structure design^[15-18], and changing the calcination environment^[19]. In these methods, inducing the formation of oxygen vacancies through redox reactions with H_2 , H_2O_2 , etc., which enhances the visible light absorption and photocatalytic properties of CeO_2 , is an effective strategy to improve the photochemical activity of CeO_2 . Ma et al.^[20] synthesized CeO_2 nanoparticles by decomposing $\text{Ce}(\text{O}_2)(\text{OH})_2$ under ultrasound and demonstrated that H_2O_2 -sonication increased the Ce^{3+} and V_{O} concentrations of CeO_2 , which resulted in a narrowing of the CeO_2 bandgap and an enhancement in photochemical activity. The synthesis of CeO_2 nanoparticles with high concentrations of Ce^{3+} and V_{O} can be achieved through annealing under a reducing atmosphere using the molten salt method, as proposed by Xu et al.^[19]. The resulting material exhibits a notable enhancement in photochemical activity, attributed to the intermediate energy state of Ce^{3+} and the generation of V_{O} within the band gap. The preparation of CeO_2 enriched with oxygen vacancies for applications in polishing compound materials (PCMP) remains challenging. Firstly, the low concentration of oxygen vacancies in CeO_2 produced via H_2O_2 -sonication is insufficient to significantly enhance its photochemical activity. Secondly, annealing at high temperatures causes the morphology of CeO_2 particles to transition from spherical to octahedral shapes, resulting in significant agglomeration that may degrade polishing quality. Therefore,

the efficient synthesis of CeO₂ particles with a uniform spherical morphology and a high concentration of oxygen vacancies has become a key area of research.

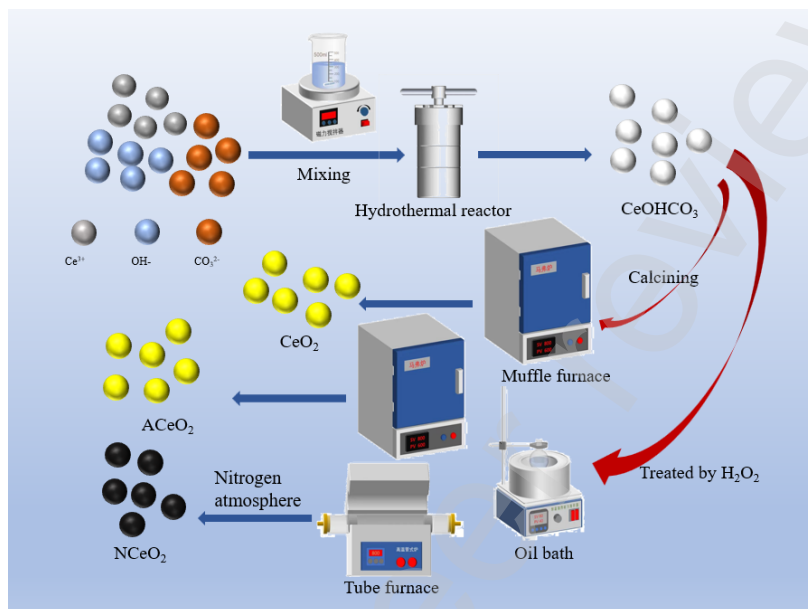
Due to the thermal decomposition property of O₂²⁻, it can introduce a high concentration of oxygen vacancies in the lattice, which makes the band gap narrower and improves the photochemical activity of the material.^[21] Therefore, in this experiment we prepared CeO₂ nanospheres with high concentrations of oxygen vacancies by decomposing Ce-O₂²⁻ under different calcination atmospheres (Air and N₂) and carried out morphological, structural, and optical characterization by using XRD, SEM, TEM, HRTEM, Raman, XPS, EPR, and UV-vis, to systematically investigate the effect of oxygen vacancies on the photochemical activity of CeO₂. First-principles calculations are used to propose mechanisms for the changes in band gap and photochemical activity of CeO₂. Based on this, the effect of oxygen vacancies on CeO₂ polishing properties is demonstrated in PCMP applications.

2. Experimental section

2.1 Synthesis

A hydrothermal method was used to prepare the CeO₂ abrasive. The specific steps were as follows: Ce(NO₃)₃·6H₂O, and 4.5 g PVP were added to 50 ml of deionized water and mixed homogeneously with vigorous stirring at room temperature, and then a certain amount of urea (molar ratio: Ce/urea = 1/60) and 60 ml of deionized water were stirred for 1h at room temperature. Subsequently, the two solutions were immediately mixed and kept stirring for 1h, then the mixed solution was loaded into a hydrothermal kettle and heated to 100 °C for 4 h. Then, the samples were subjected to centrifugation and repeated washing with ethanol and deionized water, followed by drying at 60 °C for 10 hours to obtain CeOHCO₃. Finally, the CeOHCO₃ sample was divided into two parts, and one part was annealed in air at 500 °C for 4 h to obtain CeO₂ particles, which served as a control group. The remaining portion was dispersed in an aqueous solution of hydrogen peroxide (0.75 M) and heated to 75 °C for two hours. Centrifugation was then employed to obtain the precipitate, which was subsequently dried at 60 °C for 12 hours and divided into three portions. One portion was dried and

preserved, designated as HCeOHCO_3 , while the remaining two portions were subjected to annealing at $500\text{ }^\circ\text{C}$ for four hours in air and nitrogen, respectively, to yield the products ACeO_2 and NCeO_2 . The schematic diagram of the synthesis is shown in Scheme 1.



Scheme 1. The different reaction processes of CeO_2 , ACeO_2 , and NCeO_2 methods.

2.2 Characterization

The crystal structure of CeO_2 was analyzed utilizing an X-ray diffractometer (XRD, X' Pert PRO) with $\text{Cu K}\alpha$ radiation at 40 kV and 40 mA. XRD data were obtained by continuous scanning in the range of 20° to 80° (2θ) at a scanning speed of $10^\circ/\text{min}$. Data were processed by Jade 6.5 software. The particle morphology and element distribution of sintered powder specimens were characterized by scanning electron microscopy (SEM, Gemini SEM 300) and transmission electron microscopy (TEM, JEM-2010F, JEOL). The valence states of Cerium ($\text{Ce}^{3+}/\text{Ce}^{4+}$) were characterized using the X-ray photoelectron spectroscopy (XPS, ESCALAB-250Xi) characterization was performed using $\text{Al K}\alpha$ targets excited at 1486.6 eV energy at a test pressure of 10^{-8} Pa, energy resolution ≤ 0.45 eV and spatial resolution $\leq 20\text{ }\mu\text{m}$. Raman spectra were recorded on a Thermo Nicolet 6700-NXR apparatus with an excitation source of 532 nm. Photoluminescence (PL) spectra were tracked using a fluorescence spectrophotometer (QM-8000). Ultraviolet-visible diffuse reflectance

spectra (UV–vis DRS) were collected on a Lambda750S UV-vis spectrophotometer.

2.3 DFT calculations

The density functional calculations were carried out with the Vienna ab initio simulation package (VASP).^[22, 23] The electron wave functions were described using the projector augmented wave (PAW) method. Plane waves were included up to an energetic cut-off of 500 eV.^[24] The exchange-correlation effects were treated with the generalized gradient approximation (GGA) in the form of Perdew, Burke, and Ernzerhof (PBE).^[22, 25] The effective Hubbard parameter U was employed to account for the strong on-site Coulomb repulsion amongst the localized 4f orbital for the lanthanide series elements. In this study, $U=5$ eV was applied to the 4f states of Ce, and in addition, $U=5.5$ eV was applied to the 2p states of O.^[24, 26] A $2\times 2\times 2$ supercell of the cubic fluorite structure with 96 atoms was used as the initial structural model.^[24] A cubic unit cell of C-type Ce_2O_3 can be constructed out of eight CeO_2 unit cells by increasing their volume by 3 % and removing 25 % of the oxygen atoms along four nonintersecting $\langle h111 \rangle$ diagonals.^[27]

2.4 CMP experiment

In this experiment, round quartz glass of 20 mm*2 mm size was used as the polishing substrate, and three pieces of quartz glass were glued to an aluminium alloy plate with paraffin wax around three symmetrical points on the mounting plate. CMP and PCMP tests were carried out using a precision polishing machine (UNIPOL-1200S, Shenyang Kejing Co., Ltd., China). The abrasive was selected as NCeO_2 powder to formulate a slurry with 2.5 % wt of solids. The pH of the formulated polishing solution was adjusted to 10 using 0.1 mol/L Na_2CO_3 solution and used after ultrasonic treatment for 20 min at room temperature. In the PCMP experiments, the pressure was set to 3 N, the polishing time was 4 min, and the head speed and platen speed were both 60 rpm. The slurry was irradiated using a 250 W halogen lamp as a UV source (wavelength of 365 nm) for 30 min before the PCMP. After the PCMP experiment, the wafers were repeatedly cleaned by ultrasonic treatment in ethanol and deionized water.

The polished surfaces were analyzed by AFM (Ntegra Prima SPM, NT-MDT,

Russia) atomic force microscopy in Taping mode, with a scanning range of $5.0 \times 5.0 \mu\text{m}^2$ for all AFM experiments. The data were then processed using NanoScope Analysis software to obtain the surface morphology map, the cross-section trajectory map, and surface roughness. Finally, the material removal rate (MRR) was calculated by measuring the difference in sample mass before and after polishing with a precision balance, as shown in Eq. (1)^[4].

$$\text{MRR} = \frac{\Delta m \times 10^7}{\rho \cdot S \cdot \tau} \quad (1)$$

Where Δm (g) is the mass difference of the quartz glass sample before and after CMP; ρ is the density of the quartz glass sample, which is about 2.2 g/cm^3 ; S is the total contact area of quartz glass and polishing pad (cm^2); τ is the polishing time (min).

3. Results and discussion

3.1 Structural and physicochemical properties

XRD

The crystal structures of the CeO_2 , ACeO_2 , and NCeO_2 samples were analyzed using X-ray diffraction (XRD). The results presented in Fig. 1 indicate that both ACeO_2 and NCeO_2 maintain the cubic fluorite structure of CeO_2 (PDF-34-0394), exhibiting no evidence of other impurity phases. The average grain sizes of the three samples were calculated by Scherrer's formula $D = k \lambda / \beta \cos \theta$ ^[28], based on the (111) crystal plane, where λ is the X-ray wavelength, θ is the X-ray diffraction angle, and β is the half-height width of the (111) peak. The calculated results show that the average grain sizes of NCeO_2 , ACeO_2 , and CeO_2 are 10.81 nm, 12.49 nm and 12.51 nm, respectively. The small grain sizes of NCeO_2 and ACeO_2 are attributed to the presence of a high concentration of defects at the surface or at grain boundaries, which can impede the growth of nanograins. Furthermore, the lattice constants of the (111) sample were calculated using Jade software, resulting in values of 5.412 Å, 5.409 Å, and 5.407 Å for NCeO_2 , ACeO_2 , and CeO_2 , respectively. Lattice expansion is typically associated with surface defects (Ce^{3+} and V_O).^[10] ACeO_2 and NCeO_2 samples that have undergone annealing and exhibit surface defects show significant lattice strain. To reduce lattice

strain, the lattice size of ACeO₂ and NCeO₂ samples decreases, leading to an increase in the lattice constant. In the case of ACeO₂, the surface defects created during annealing are compensated by atmospheric oxygen, resulting in a smaller increase in the lattice constant.

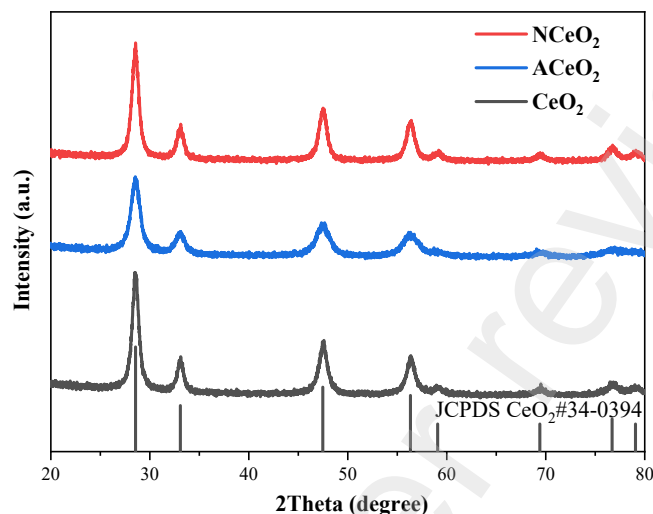


Fig 1. The XRD patterns of CeO₂, ACeO₂, and NCeO₂ with PDF cards of CeO₂ were given as reference.

SEM and TEM

Studies have shown that interfaces and grain boundaries serve as active sites for the formation of Ce³⁺ and V_o in CeO₂ systems. The likelihood of defect formation near grain boundaries is influenced by the local atomic structure and the orientation of nearby particles.^[10] As illustrated in Fig. 2 (a), (b), and (c), the spherical morphology and uniform size of ACeO₂ and NCeO₂ remain consistent. As can be observed in the enlarged images of the red areas in Fig. 2 (e), (f), and (g), the lattice stripes of CeO₂ are visible. It can be seen that there are significant overlapping folds between the lattice stripes of NCeO₂ (indicated by the red arrows), which is a consequence of the presence of oxygen vacancy defects at the grain boundaries, resulting in the misalignment of the lattice stripes.^[29] Subsequent measurements of CeO₂, ACeO₂, and NCeO₂ showed a crystal plane spacing of 0.306 nm, 0.308 nm, and 0.313 nm, respectively, corresponding to the CeO₂ (111) crystal plane. According to Eq. (2), the observed increase in crystal plane spacing is directly related to the increase in lattice constant, as determined by

XRD analysis. Fig. 2 (d), and (h) show comparative high-resolution transmission electron microscopy (HRTEM) images of CeO₂ and NCeO₂. The red dashed circles in the figures indicate that, unlike CeO₂, NCeO₂ displays fuzzy lattice stripes in the edge region, which are attributed to the formation of oxygen vacancy defects.^[30]

$$d = \frac{a}{(h^2 + k^2 + l^2)} \quad (2)$$

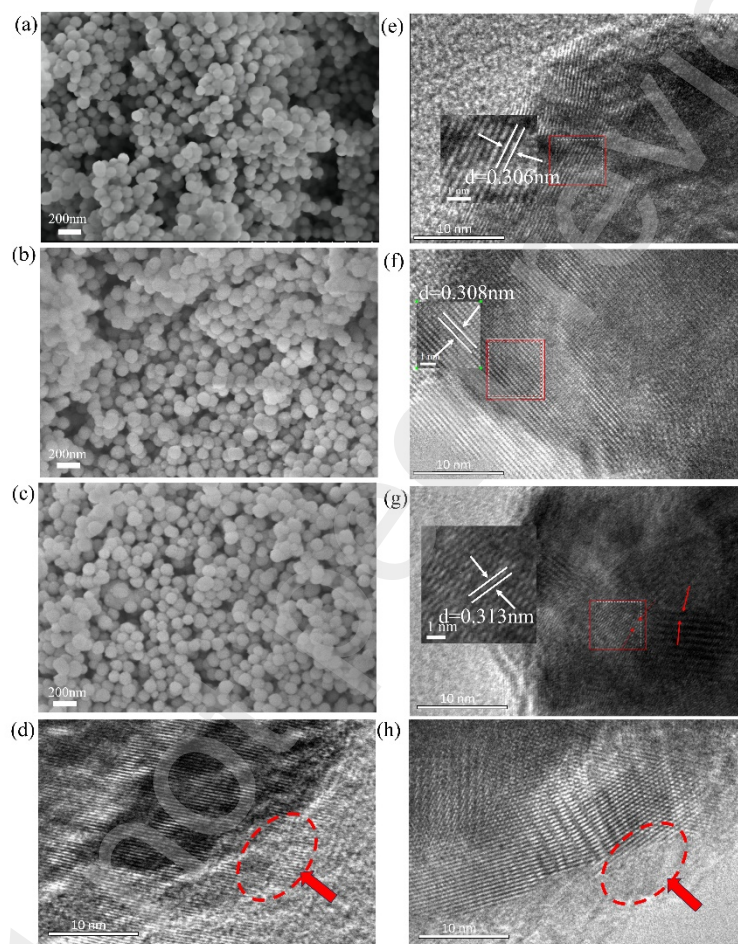


Fig 2. SEM and HRTEM images of (a, d, e) CeO₂, (b, f) ACeO₂, and (c, g, h) NCeO₂ samples.

Raman

The Raman spectra of each sample are shown in Fig. 3. The spectrum shown in Fig. 3(a) reveals that the H₂O₂-treated precursor CeOHCO₃ displays a distinct vibrational peak at approximately 830 cm⁻¹, highlighted by the red dashed box. This peak corresponds to the characteristic Ce-O₂²⁻. The observed peak is attributed to the intermediate Ce(O₂)(OH)₂ generated by the redox reaction between H₂O₂ and Ce³⁺, as detailed in Eq. (3).^[31] As illustrated in Fig. 3 (b), the F_{2g} characteristic peak of CeO₂

appears at 465 cm⁻¹ for the sample annealed according to Eq. (4). NCeO₂ exhibits a pronounced vibrational peak near 600 cm⁻¹, as shown in the inset of Fig. 3 (b). Conversely, the peak intensity of ACeO₂ that was annealed in air is diminished. In general, an increase in the intensity ratio of I_{600}/I_{465} is indicative of an increase in V_o content. The oxygen vacancy rates were calculated to be CeO₂ (0.02), NCeO₂ (0.044), and ACeO₂ (0.028) for each sample. Furthermore, the Raman vibrational mode near 1174 cm⁻¹ in the right inset of Fig. 3 (b) is correlated with the O-O stretching vibrational mode of the superoxide radical $\cdot O_2^-$,^[32] and it can be observed that the intensity of this peak is higher in both ACeO₂ and NCeO₂ than that of CeO₂. The formation of $\cdot O_2^-$ is due to the interaction of the adsorbed oxygen on the surface with the electrons trapped in the oxygen vacancies, indicating that the oxygen defects are higher in both ACeO₂ and NCeO₂.

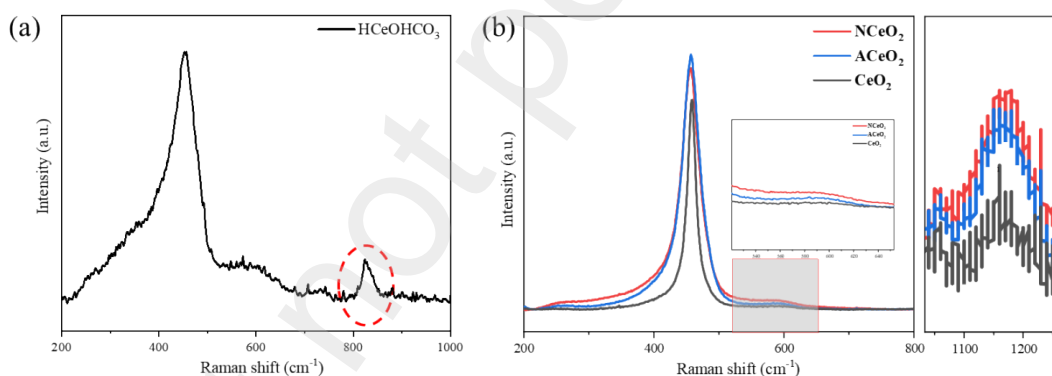
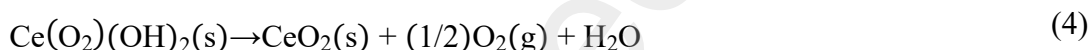
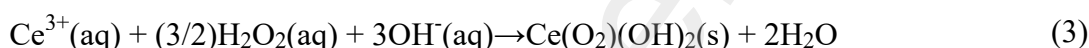


Fig 3. Raman spectra of (a) HCeOHCO₃; (b) CeO₂, ACeO₂, and NCeO₂.

XPS

In order to gain a deeper understanding of the oxygen vacancy concentration variations of the samples, X-ray photoelectron spectroscopy (XPS) was employed to characterize the valence information of the corresponding cerium elements of the three abrasives. The data were analyzed using a nonlinear peak fitting method for the Ce 3d spectra, as illustrated in Fig. 4 (a). The Ce 3d energy level comprises two pairs of spin orbitals, 3d_{3/2} and 3d_{5/2}. The peaks in the Ce 3d core energy peaks, modulated by the

fluctuations in the Ce 4f electronic states, reflect the variations between Ce^{3+} and Ce^{4+} .^[33] The Ce3d core level spectra were further analyzed using nonlinear peak fitting methods. The peaks corresponding to the spin-orbit $3d_{3/2}$ and $3d_{5/2}$ are labeled as u and v, respectively. The peaks labelled as u''' , u'' , u, v''' , v'' , v represent Ce^{4+} , while peaks labelled as u' , u_0 , v' , v_0 correspond to Ce^{3+} . The presence of both Ce^{3+} and Ce^{4+} peaks across all samples indicates a mixed valence state of +3 and +4 within the CeO_2 samples. The valence state of Ce was semi-quantitatively analyzed using the peak area ratio, as described Eq. (5),^[33] and the results are shown in Fig. 4 (b). The Ce^{3+} concentration of CeO_2 abrasive was 22.32 %, and for ACeO_2 and NCeO_2 abrasives, it rose to 27.31 % and 33.59 %, respectively, which indicates that thermal decomposition of O_2^{2-} enhances Ce^{3+} concentration, supporting the preliminary findings from Raman analysis. Fig. 4 (c) illustrates the nonlinear fitting of the O 1s fine spectra of the abrasives. In this context, O1 is typically defined as surface-adsorbed oxygen, O2 as adsorbed oxygen at oxygen vacancies, and O3 as lattice oxygen. A comparison of the O1 peak areas among the three samples indicated that the O1 surface-adsorbed oxygen peak area for ACeO_2 represented the highest proportion. This result supports the hypothesis that oxygen from the surrounding environment can offset oxygen vacancies. Furthermore, the lattice peaks of NCeO_2 and ACeO_2 exhibit a shift towards higher binding energies, indicative of a reduction in the electron density of lattice oxygen. This phenomenon is associated with an increase in the concentration of oxygen defects in CeO_2 .^[18] The V_δ content was calculated according to Eq. (6)^[34], and the V_δ contents of CeO_2 , ACeO_2 and NCeO_2 were 26.51 %, 45.82 % and 48.51 %, respectively. According to Eq. (7-9),^[35] O_2^{2-} decomposition during calcination produces O_2 , which generates oxygen defects in the lattice because O_2 can be released rapidly. The decomposition environment is rich in O^{2-} ions, which hinders the reduction reaction of Eq. (9). As the reaction proceeds, the oxidation reaction of Eq. (8) is more likely to occur, increasing the V_δ concentration. The storage and release of oxygen in CeO_2 are optimized when the temperature is exceeding 150 °C. At lower temperature, the rate of surface oxygen diffusion decreases, facilitating its retention within the lattice structure.^[20] Consequently, once the decomposition reaction is complete, oxygen from the air fills the vacancies in the lattice

during the cooling process. This results in a decreased rate of increase in the V_{δ} concentration of $ACeO_2$. Furthermore, comparing $ACeO_2$ and $NCeO_2$ revealed that the rate of increase in V_{δ} concentration diminished under altered atmospheric conditions. This indicates that the primary factor contributing to the observed increase in V_{δ} concentration is O_2^{2-} decomposition.

$$\frac{Ce^{3+}}{Ce^{3+} + Ce^{4+}} = \frac{\text{area}(v_0, u_0, v', u')}{\text{total area}} \quad (5)$$

$$\frac{V_{\delta}}{O_{\text{lattice}} + V_{\delta} + O_{\text{absorption}}} = \frac{\text{area}(O^2)}{\text{total area}} \quad (6)$$

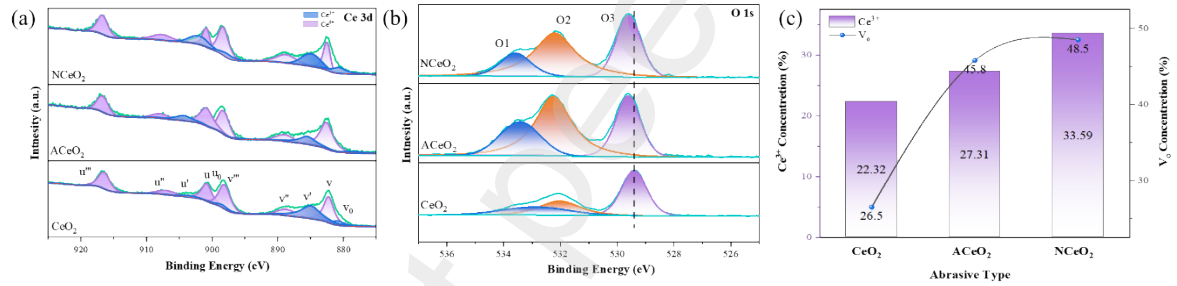


Fig 4. XPS spectroscopic spectra of the CeO_2 , $ACeO_2$, and $NCeO_2$ samples: (a) Ce 3d; (b) O 1s; (c) the concentration of Ce^{3+} and V_{δ} .

UV

To evaluate the effect of oxygen vacancies on the band gap of CeO_2 , we examined the optical properties of the three samples using UV-vis spectroscopy. Fig. 5 (a) illustrates that the wavelengths of $ACeO_2$ and $NCeO_2$ display a significant red shift, with the absorption tail of $NCeO_2$ extending into the visible region, which is not observed in CeO_2 . The extended absorption tail in $NCeO_2$ can be attributed to the presence of high concentrations of Ce^{3+} and V_{δ} .^[36] The optical bandgap of the samples can be evaluated further on the basis of the Kubel-Munk function, and the corresponding plots of $(ah\nu)^2$ versus $(h\nu)$ are shown in Fig. 5 (b), yield bandgaps of CeO_2 (3.08 eV), $NCeO_2$ (2.86 eV), and $ACeO_2$ (2.98 eV). The individual samples

displayed a redshift in the UV absorption curves and a narrowing of the bandgap, attributed to the increased concentrations of Ce^{3+} and V_δ . These results align with the findings from XPS and Raman analysis.

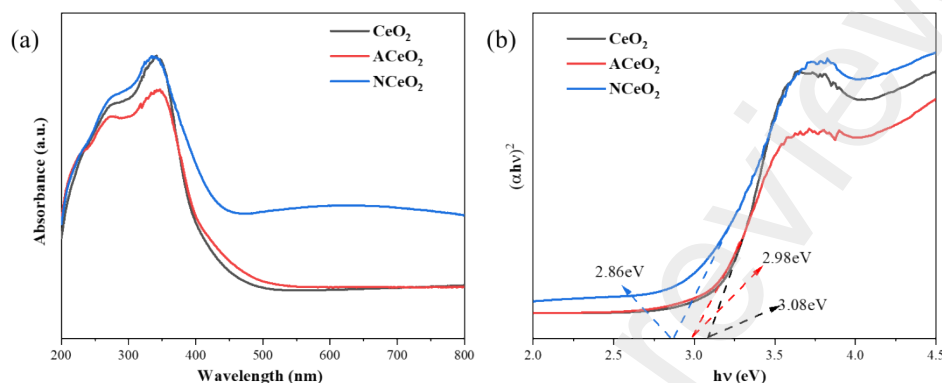


Fig 5. UV–visible diffuse reflectance spectra (a), and the energy band gap (b) of the as-prepared CeO_2 , ACeO_2 , and NCEO_2 samples.

PL

The photoluminescence (PL) spectral characterization of materials is commonly used to evaluate the efficiency of the complexation of photogenerated electrons (e^-) and holes (h^+). Research indicates that a reduction in the rate of e^- and h^+ complexation increases the lifetime of photogenerated charge carriers, thereby enhancing the material's photochemical activity.^[37] Furthermore, this is supported by the observed decrease in peak intensities in the PL spectra. Fig. 6 (a) illustrates the PL spectra of all the CeO_2 samples. From Fig. 6 (a), it can be observed that there is a clear peak between wavelengths of 480-510 nm, corresponding to the defect energy level between the Ce 4f and O 2p bands.^[38] A significant decrease in the PL intensity of NCEO_2 compared to CeO_2 was observed. In contrast, the PL intensity of ACeO_2 was higher than that of CeO_2 . The PL intensity could be affected by the presence of both radiative and non-radiative defects, located within the bulk and on the surface of the material. The presence of defects within the body results in an increase in PL intensity, whereas defects on the surface of the material lead to a reduction in PL intensity.^[10] In conclusion, NCEO_2 possesses a high density of oxygen defects on its surface. These

defect centers function as non-radiative complexes, enhancing the segregation and transport of photogenerated electron-hole pairs, thereby suppressing the PL intensity of NCeO_2 while simultaneously improving its photochemical activity. In contrast, for ACeO_2 , the PL intensity is primarily influenced by the defects within the lattice, which compensate for the adsorbed oxygen on the surface, resulting in an increase in PL intensity. Fig. 6 (b) depicts the EPR signals of CeO_2 , ACeO_2 , and NCeO_2 nanostructures. Fig. 6 (b, c) demonstrates that all three structures exhibit signal peaks at 3515 G and $g=2.00$, which are attributed to Ce^{3+} in the samples.^[39] In this case, it can be observed that the intensity of the Ce^{3+} signal is higher for both ACeO_2 and NCeO_2 than for CeO_2 ; this increase in intensity is due to the formation of defects in CeO_2 as a result of CeO_2 decomposition and the reduction of Ce^{4+} to Ce^{3+} . The analytical results indicate that Ce^{3+} and V_{O} effectively enhance the transfer of photogenerated electrons, inhibit the complexation of photogenerated carriers, and improve the photochemical activity of CeO_2 .

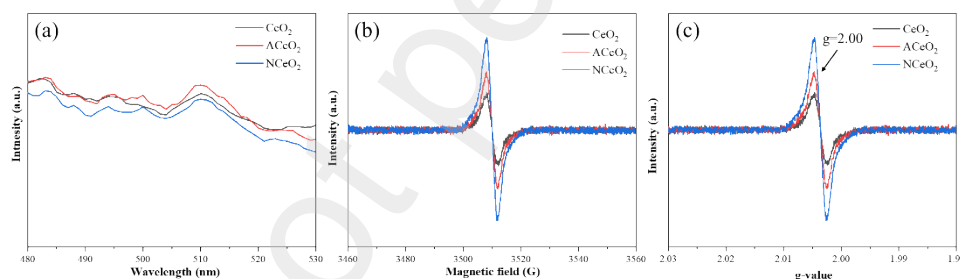


Fig 6. (a) Photoluminescence, (b) EPR, and (c) g -value spectra of CeO_2 , ACeO_2 , and NCeO_2 samples.

DFT

This study further explores the effect of oxygen vacancies on the electronic properties of CeO_2 through the use of first-principles calculations. This study examines the density of states (DOS) near the Fermi energy level, which primarily reflects the electronic structure of CeO_2 . Fig. 7 illustrates the DOS of systems containing CeO_2 with different oxygen vacancy concentrations. As shown in Fig. 7 (a), the band gap of CeO_2 is approximately 2.38 eV. When an oxygen vacancy is introduced into the CeO_2 lattice, the density of CeO_2 is shifted to the low-energy state as can be seen in Fig. 7 (b), which

is due to the introduction of the oxygen vacancy,^[24, 33] and the band gap width is slightly narrowed to 2.31 eV. In contrast to the preceding two cases, 25 % oxygen vacancies are incorporated into the CeO₂ lattice in a particular manner (as illustrated in Fig. 7 (e)), resulting in the emergence of new bandgap states in proximity to the Fermi energy level. This phenomenon leads to a narrowing of the band gap, as depicted in Fig. 7 (c). The PDOS diagram shown in Fig. 7 (d) that the gap state is mainly from the Ce 4f state, which indicates that the Ce 4f orbital is partially occupied by two electrons generated after the formation of the oxygen vacancy. And the electron of Ce 4f state is localized on the Ce ion around the oxygen vacancy, which will promote the two neighboring Ce⁴⁺ reduction to Ce³⁺. Fig. 7 (f) shows the impact of V_o concentration on the energy band structure of CeO₂, as derived from the DOS variation. In the case of a low oxygen vacancy concentration, the defect level has a negligible effect on the band gap width (as illustrated in Fig. 7 (b)).^[24] When the concentration of oxygen vacancies in CeO₂ increases further, a new energy gap state emerges near the Fermi energy level (as shown in Fig. 7 (c)). This phenomenon results in a narrowing of the CeO₂ band gap and an enhancement of its photochemical activity. This analysis effectively explains the redshift observed in the absorption edge of the UV spectrum presented in Fig. 5 (a).

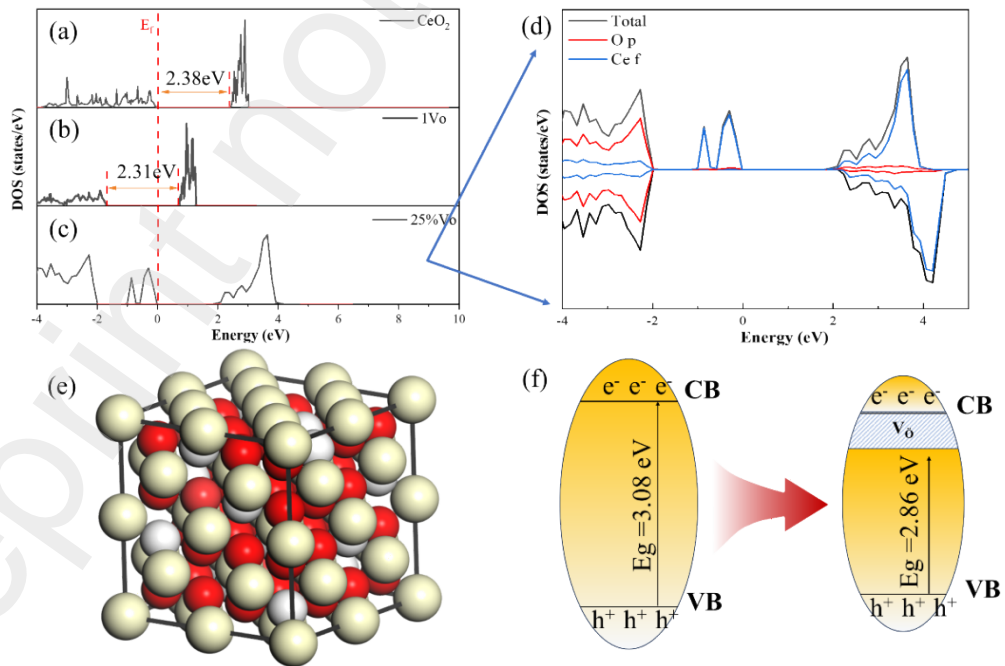


Fig 7. Calculated density of electronic states (DOS) for CeO₂ (in a 2*2*2 supercell). (a) Defect-free, stoichiometric crystal, (b) The model has one oxygen vacancy, (c) Model with 25 % oxygen

vacancy, (d) The PDOS for CeO₂ with 25 % oxygen vacancy, (e) Lattice unit cells for Ce₂O₃, (f) Illustration of the Energy Bands for CeO₂ with Oxygen Vacancy Concentration and the Photoinduced Electronic Processes.

Fig. 8 illustrates the schematic structure of the self-doped CeO₂ system. The free electrons generated within the CeO₂ system are readily stored due to the presence of Ce 4f orbitals, which are responsible for the conversion of Ce⁴⁺ to Ce³⁺.^[40] As shown in Fig. 8 (a), O₂²⁻ decomposes during calcination and oxidizes to O₂, which forms oxygen vacancies in the lattice due to the rapid release of O₂.^[35] The spillage of molecular oxygen releases two free electrons in the vacancies to maintain electrical neutrality as shown in Fig. 8 (b). It is noteworthy that Ce⁴⁺ around the oxygen vacancies can trap electrons according to Eq. (10)^[33], leading to the transformation of Ce⁴⁺ to Ce³⁺ as shown in Fig. 8 (c).

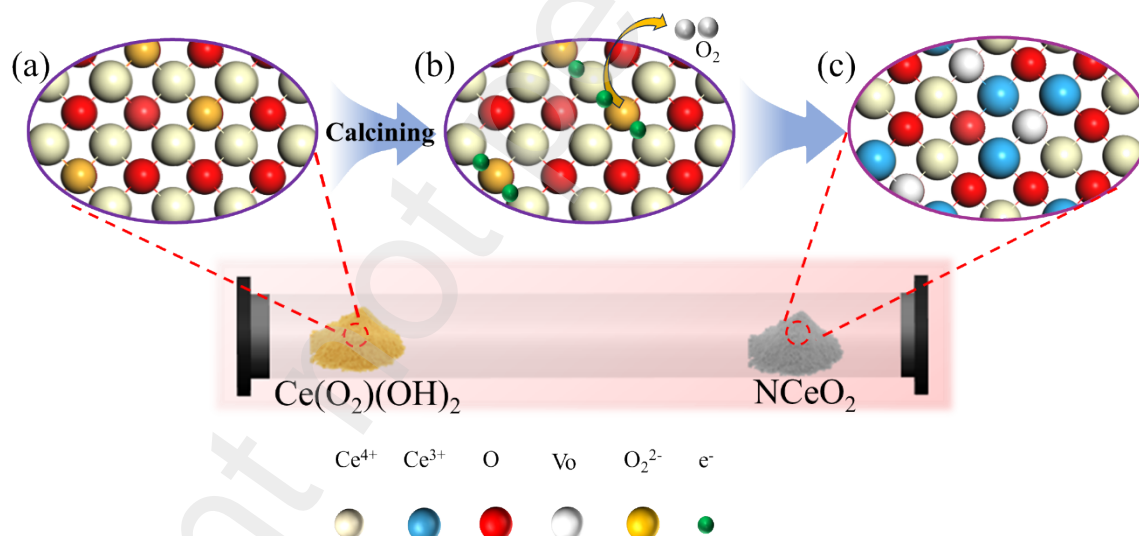


Fig 8. Schematic diagram of the structural evolution of CeO₂ crystal decomposed with O₂²⁻.

3.2 Polishing performances

3.2.1 Surface analysis and removal efficiency

Surface quality and removal efficiency are the key indicators for evaluating the performance of abrasives. In this experiment, high-resolution atomic force microscopy was utilized to observe the evolution of the surface morphology of substrate after polishing, including two-dimensional (2D) height images, three-dimensional (3D)

images, as shown in Fig. 9 (a-f). For the cross-section profile analysis, the diagonal line in the 2D-AFM height image was selected for scanning measurement and further comparison, X denotes the length of the line profile, the Z-axis denotes the depth of the line profile, and the improvement of the surface quality can be evidenced by the reduction of the roughness of the line profile,^[36] as shown in Fig. 9 (g-i).

Combined with the above characterization of the crystal structure and photochemical activity of the three abrasives, the NCeO₂ abrasive was selected for the CMP and PCMP processes, respectively. As illustrated Fig. 9 (a, d), it can be seen that the surface before polishing is highly undulating with a large number of rough peaks. The maximum valley depth (MVD) of the pre-polished surface is about 4.812 nm and the maximum peak height (MPH) is about 5.212 nm as observed from Fig. 9 (g). From Fig. 9 (h), the maximum valley depth (MVD) of the substrate after CMP treatment is 0.981 nm, the maximum peak height (MPH) is 1.482 nm, and a large number of nano-sized roughness peaks still exist on the surface of the substrate after CMP, as can be seen by the AFM images in Fig. 9 (b, e). This is attributable to the insufficient hardness of NCeO₂ and its inadequate mechanical action in the conventional CMP process. Fig. 9 (i) depicts that the maximum valley depth (MVD) of the SiO₂ surface after PCMP treatment is 0.521 nm, while the maximum peak height (MPH) is 0.744 nm. A comparison of Fig. 9 (b, c) and (e, f) demonstrates that the majority of the roughness peaks associated with defects on the substrate surface were effectively removed following PCMP polishing. These observations indicate a notable enhancement in surface quality.

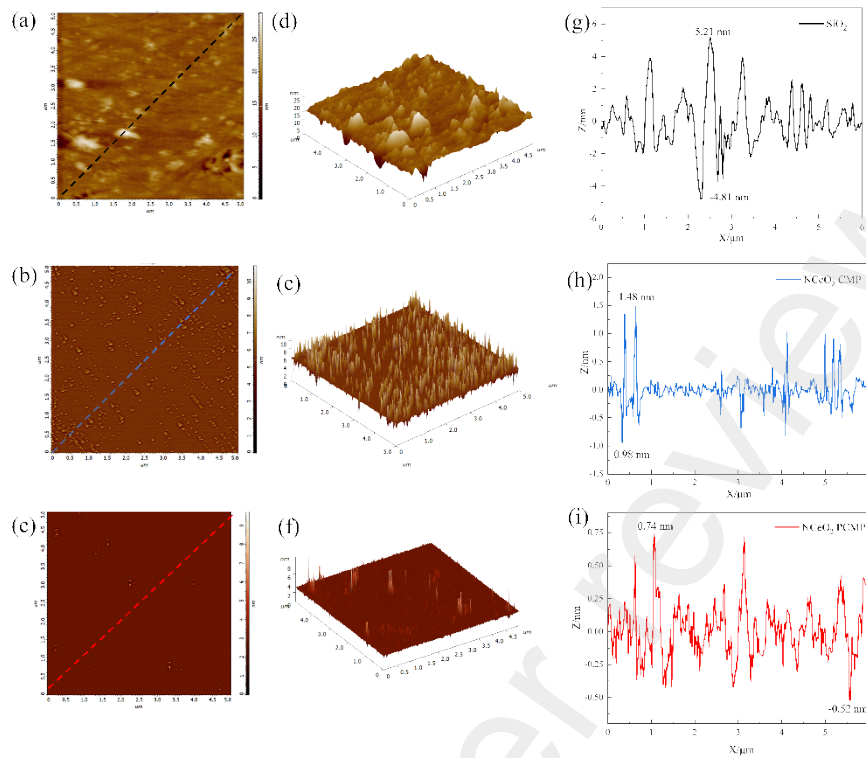


Fig 9. 2D-, 3D-AFM images and the corresponding contour line curve of the quartz glass: (a, d, g) before polishing; (b, e, h) after CMP; (c, f, i) after PCMP.

As illustrated in Fig. 10, the bar chart demonstrates that Ra and RMS of substrates before polishing were 0.957 nm and 1.263 nm, respectively, within $5.0 \times 5.0 \mu\text{m}^2$ area. Following CMP and PCMP, the Ra of substrate was reduced to 0.471 nm and 0.217 nm, respectively, while the RMS was 0.773 nm and 0.279 nm. After PCMP, Ra and RMS were reduced by 53.9%, 71.8 %, and 67.7%, 80.1 %, respectively, in comparison to the $\text{N}\text{CeO}_2(\text{CMP})$, and the previously reported commercial CeO_2 sample.^[41]

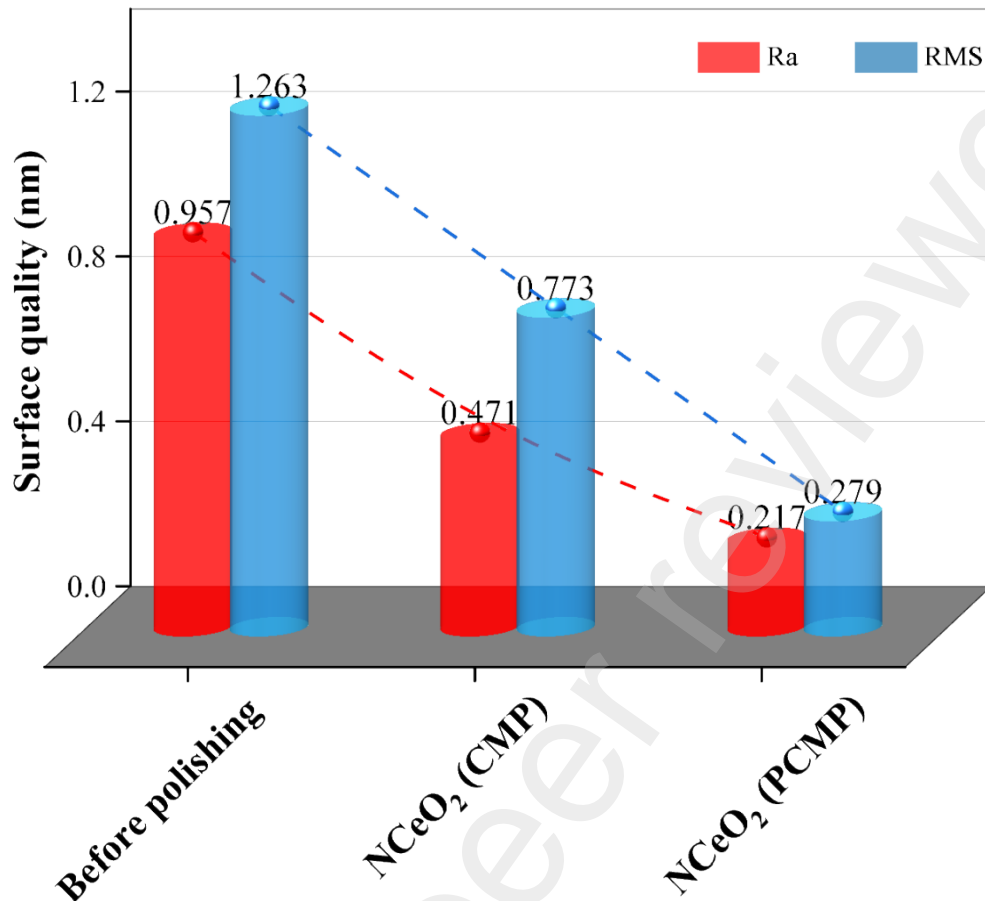


Fig 10. The surface roughness after CMP and PCMP.

As illustrated in Fig. 9 and 10, the as-prepared abrasives were capable of markedly enhancing the surface quality, resulting in an atomically smooth and scratch-free surface by comparison with the original substrate. In order to reduce the variability of the polishing results, three random measurement locations were selected on the polishing plane of each sample and the surface roughness (Ra), and the root mean square roughness (RMS) roughness results were averaged and listed in Table 1.

The removal of material is another key indicator for the evaluation of the polishing performance of abrasive particles. In this work, the MRR-PCMP of the prepared NCeO₂ abrasive was approximately 361.89 nm/min, representing a 24.92 % improvement over the CMP (without UV irradiation, approximately 289.52 nm/min). Based on the results of the above analysis, it is shown that the proposed abrasive for PCMP achieves almost scratch-free and highly flattened surfaces with very low roughness.

Table 1. Surface characteristics of the substrates after CMP and PCMP with NCeO₂.

Before polishing	Ra (nm)	RMS (nm)
1	0.969	1.234
2	0.968	1.242
3	0.933	1.315
Average	0.957±	1.263±
	0.02	0.03
NCeO₂(CMP)	Ra (nm)	RMS (nm)
1	0.471	0.729
2	0.492	0.877
3	0.447	0.714
Average	0.471±	0.773±
	0.02	0.06
NCeO₂(PCMP)	Ra (nm)	RMS (nm)
1	0.207	0.270
2	0.229	0.293
3	0.216	0.274
Average	0.217±	0.279±
	0.007	0.01

3.2.2 Proposed PCMP Mechanism

In the process of polishing, the OH⁻ in the alkaline slurry initially reacts with the Si-O-Si bonds on the SiO₂ surface. Subsequently, the resulting Si(OH)₄ hydration layer can be removed by induced shear (or friction) from the granular abrasive and pad roughness. As in the chemical tooth model proposed by Cook,^[1] the chemically reactive layer can be removed by solid-state frictional chemical reactions occurring at the CeO₂-SiO₂ interface.

Fig. 11 presents a schematic diagram of the photo-oxidation mechanism of CeO₂. In contrast to the conventional CMP, in the PCMP system, when CeO₂ is irradiated by UV light, photogenerated electrons (e⁻) are excited from the valence band (VB) to the conduction band (CB), and a photogenerated hole (h⁺) is left at the VB position. For the wide bandgap semiconductor CeO₂, photogenerated electrons tend to complex with holes due to the Coulomb force associated with the larger bandgap. This interaction hinders the effectiveness of the photocatalytic oxidation process, as shown in Fig. 11

(a). In the newly proposed NCeO₂ system shown in Fig. 11 (b), a high concentration of oxygen vacancies leads to the emergence of a new gap state near the Fermi energy level of CeO₂, which narrows the overall band gap. Combined with the UV spectra and Eqs. (11), and (12),^[3] where χ is the absolute electronegativity of CeO₂ (5.57 eV), and E_e is the energy of free electrons on the hydrogen scale (NHE, 4.5 eV).^[3] Calculations give E_{VB} and E_{CB} of 2.5 eV and -0.36 eV for NCeO₂, respectively. In this system, when CeO₂ is irradiated by UV light, the photogenerated electron (e^-) can migrate from the VB of CeO₂ to the CB, and the photogenerated hole (h^+) can be retained in the VB. The resulting h^+ can then react with OH⁻ or H₂O to produce a strong oxidizing \cdot OH radical. The e^- migrating to the CB to be excited can trap the dissolved oxygen in the slurry to produce \cdot O²⁻ radicals.^[42] Consequently, the NCeO₂ system effectively reduces the complexation rate of photo-generated electron-hole (e^-/h^+) pairs, consistent with the findings from PL spectral analysis (Fig. 6). According to the literature^[43], the generated reactive species (\cdot OH, \cdot O²⁻, etc.), during the PCMP process, promote the formation of the chemically reactive layer Si(OH)₄, which in turn facilitates the material removal.

$$E_{VB} = \chi - E_e + 1/2 E_g \quad (11)$$

$$E_{CB} = E_{VB} - E_g \quad (12)$$

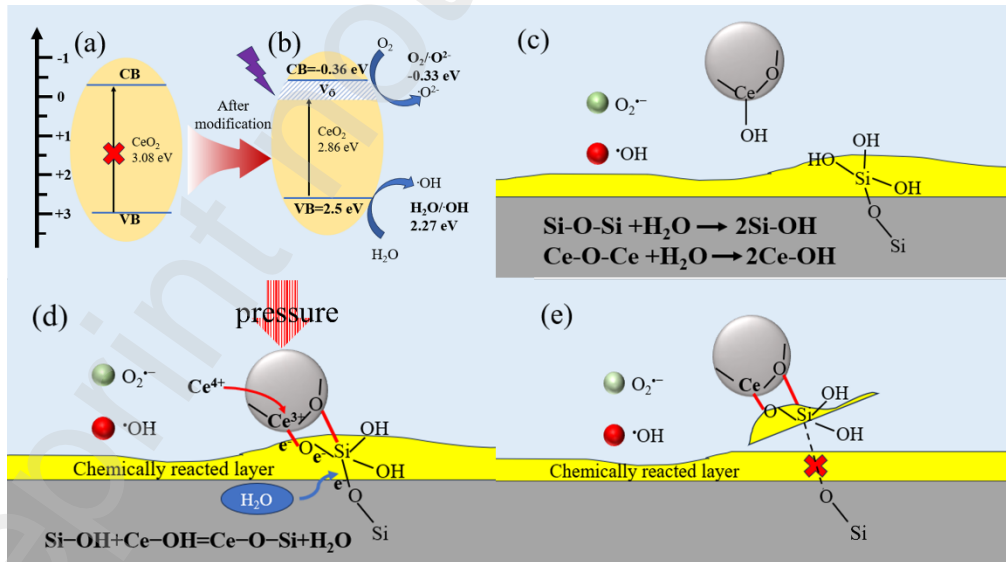


Fig 11. (a-b) Charge-transfer routes in NCeO₂ photocatalyst; (c-e) PCMP mechanism diagram of NCeO₂ samples.

Fig. 11 (c-e) illustrates a schematic representation of the polishing process for

PCMP, which is divided into three distinct phases: a chemical softening phase, a mechanical removal phase, and a polishing completion phase.^[38, 44] In the initial phase, robust oxidation species ($\cdot\text{OH}$, $\cdot\text{O}^{2-}$) generated by UV irradiation oxidize SiO_2 into $\text{Si}(\text{OH})_4$ within a humid environment. This reaction produces a malleable layer of $\text{Si}(\text{OH})_4$ that can be easily removed, as highlighted by the yellow region marked with a red arrow in the figure. In the second stage, applying mechanical stress leads to the formation of a -Ce-O-Si- structure between CeO_2 and SiO_2 . This facilitates the effective removal of SiO_2 during the polishing process. Finally, in the third stage, an exceptionally smooth SiO_2 surface is achieved through the reaction and friction between SiO_2 and the polishing pad.

4. Conclusions

In this study, we successfully prepared CeO_2 with a high concentration of oxygen vacancies by introducing these vacancies into the CeO_2 lattice via self-doping. This was achieved through a straightforward oxidation reaction between H_2O_2 and Ce^{3+} . This method differs from traditional doping techniques, as it does not introduce any impurity elements. Our findings indicate that a substantial concentration of oxygen vacancies acts as a trap center and facilitates the generation of novel defect energy levels in CeO_2 , close to the Fermi energy level. Consequently, this leads to a reduction in the band gap and an increase in photochemical oxidation activity. High-resolution AFM results reveal that ultra-smooth and high-quality surfaces can be obtained, exhibiting R_a values of 0.217 nm and RMS values of 0.274 nm within $5.0 \times 5.0 \mu\text{m}^2$ area under PCMP conditions. R_a and RMS were reduced by 53.9 % and 67.7 %, respectively, in comparison to the $\text{NCeO}_2(\text{CMP})$. As anticipated, The NCeO_2 abrasive further provided 24.94 % increment of RR-PCMP by comparison with RR-CMP (361.89 nm/min vs 289.52 nm/min). The increase in MRR-PCMP is attributed to two factors: the generation of highly reactive oxygen species ($\cdot\text{OH}$, $\cdot\text{O}^{2-}$, etc.), which promotes the formation of chemically reactive soft layers in the slurry. Additionally, the increased concentration of Ce^{3+} on the CeO_2 surface accelerates the formation and breakage of Ce-O-Si bonds, thereby improving polishing efficiency. In conclusion, the NCeO_2 used

in this study, characterized by a high concentration of oxygen vacancies, exhibited favorable PCMP properties. The findings will serve as a theoretical and experimental foundation for CeO₂-based abrasive polishing.

References

- [1] Cook, L. M., CHEMICAL PROCESSES IN GLASS POLISHING, *J. Non-Cryst. Solids.* 120 (1990), 152-171.[http://doi.org/10.1016/0022-3093\(90\)90200-6](http://doi.org/10.1016/0022-3093(90)90200-6).
- [2] Wang, L. Y., Zhang, K. L., Song, Z. T., Feng, S. L., Ceria concentration effect on chemical mechanical polishing of optical glass, *App. Surf. Sci.* 253 (2007), 4951-4954.<http://doi.org/10.1016/j.apsusc.2006.10.074>.
- [3] Wang, M. H., Mu, Z. Y., Wang, T. Y., Chen, Y., Chen, A. L., Double-layered core-shell heterostructures of mSiO₂@CdS@CeO₂ abrasive systems toward photochemical mechanical polishing (PCMP) applications, *App. Surf. Sci.* 614 (2023).<http://doi.org/10.1016/j.apsusc.2022.156274>.
- [4] Chen, A. L., Duan, Y. H., Mu, Z. Y., Cai, W. J., Chen, Y., Meso-silica/Erbium-doped ceria binary particles as functionalized abrasives for photochemical mechanical polishing (PCMP), *App. Surf. Sci.* 550 (2021).<http://doi.org/10.1016/j.apsusc.2021.149353>.
- [5] Chen, A. L., Wang, T. Y., Chen, Y., Wang, S. R., Chen, Y., Development of polystyrene/polyaniline/ceria (PS/PANI/CeO₂) multi-component abrasives for photochemical mechanical polishing/planarization applications, *App. Surf. Sci.* 575 (2022).<http://doi.org/10.1016/j.apsusc.2021.151784>.
- [6] Chen, Y., Zhong, L. N., Chen, A. L., Fu, M., Lu, X. W., Highly dispersed Gd-CeO₂ nanocrystals supported on mesoporous silica composite particles towards photochemical (photo-assisted chemical) mechanical polishing, *Ceram. Int.* 49 (2023), 16932-16943.<http://doi.org/10.1016/j.ceramint.2023.02.055>.
- [7] Chahal, S., Rani, N., Kumar, A., Kumar, P., UV-irradiated photocatalytic performance of yttrium doped ceria for hazardous Rose Bengal dye, *App. Surf. Sci.* 493 (2019), 87-93.<http://doi.org/10.1016/j.apsusc.2019.06.284>.
- [8] He, Y., Yuan, Z. W., Song, S. Y., Gao, X. J., Deng, W. J., Investigation on Material Removal Mechanisms in Photocatalysis-Assisted Chemical Mechanical Polishing of 4H-SiC Wafers, *Int. J. Precis. Eng. Man.* 22 (2021), 951-963.<http://doi.org/10.1007/s12541-021-00494-1>.
- [9] Choudhury, B., Choudhury, A., Ce³⁺ and oxygen vacancy mediated tuning of structural and optical properties of CeO₂ nanoparticles, *Mater. Chem. Phys.* 131 (2012), 666-671.<http://doi.org/10.1016/j.matchemphys.2011.10.032>.
- [10] Choudhury, B., Chetri, P., Choudhury, A., Oxygen defects and formation of Ce³⁺ affecting the photocatalytic performance of CeO₂ nanoparticles, *RSC Adv.* 4 (2014), 4663-4671.<http://doi.org/10.1039/c3ra44603d>.
- [11] Fan, Y. Y., Jiao, J., Zhao, L., Tang, J. K., Preparation of lanthanide-doped polystyrene/CeO₂ abrasives and investigation of slurry stability and photochemical

- mechanical polishing performance, *Colloid. Surface. A.* 656 (2023).<http://doi.org/10.1016/j.colsurfa.2022.130508>.
- [12] Kim, K., Yi, D. K., Paik, U., Increase in Ce^{3+} Concentration of Ceria Nanoparticles for High Removal Rate of SiO_2 in Chemical Mechanical Planarization, *ECS. J. Solid. State Sc.* 6 (2017), 681-685.<http://doi.org/10.1149/2.0371709jss>.
- [13] Liu, Y. L., Zhang, R. L., Study of doped mesoporous ceria with tailored oxygen vacancies for enhances activity for ethylbenzene oxidation application, *Colloid. Surface. A.* 603 (2020).<http://doi.org/10.1016/j.colsurfa.2020.125163>.
- [14] Liyanage, A. D., Perera, S. D., Tan, K., Chabal, Y., Balkus, K. J., Synthesis, Characterization, and Photocatalytic Activity of Y-Doped CeO_2 Nanorods, *ACS Catal.* 4 (2014), 577-584.<http://doi.org/10.1021/cs400889y>.
- [15] Gao, Q., Cui, Y., Zhang, H., Wang, S., Liu, B., Liu, C., Construction of Z-scheme 1D CdS nanorods/2D ultrathin CeO_2 nanosheets toward enhanced photodegradation and hydrogen evolution, *Sep. Purif. Technol.* 274 (2021).<http://doi.org/10.1016/j.seppur.2021.119116>.
- [16] Khan, A. J., Gao, L., Sajjad, M., Khan, S., Mateen, A., Ghaffar, A., Malik, I. A., Liao, X., Zhao, G., Synthesis of heterostructured ZnO-CeO_2 nanocomposite for supercapacitor applications, *Inorg. Chem. Commu.* 159 (2024).<http://doi.org/10.1016/j.inoche.2023.111794>.
- [17] Liang, X., Wang, P., Gao, Y., Huang, H., Tong, F., Zhang, Q., Wang, Z., Liu, Y., Zheng, Z., Dai, Y., Huang, B., Design and synthesis of porous M-ZnO/CeO_2 microspheres as efficient plasmonic photocatalysts for nonpolar gaseous molecules oxidation: Insight into the role of oxygen vacancy defects and M=Ag, Au nanoparticles, *Appl. Catal. B* 260 (2020), 118151.<http://doi.org/https://doi.org/10.1016/j.apcatb.2019.118151>.
- [18] Pu, Y., Luo, Y., Wei, X., Sun, J., Li, L., Zou, W., Dong, L., Synergistic effects of Cu_2O -decorated CeO_2 on photocatalytic CO_2 reduction: Surface Lewis acid/base and oxygen defect, *Appl. Catal. B, Environ.* 254 (2019), 580-586.<http://doi.org/10.1016/j.apcatb.2019.04.093>.
- [19] Ma, J. H., Xu, N., Luo, Y. X., Liu, Q., Pu, Y. P., Defect generation and morphology transformation mechanism of CeO_2 particles prepared by molten salt method, *Ceram. Int.* 49 (2023), 4929-4943.<http://doi.org/10.1016/j.ceramint.2022.10.007>.
- [20] Ma, C., Fu, J., Chen, J., Wen, Y., Fasan, P. O., Zhang, H., Zhang, N., Zheng, J., Chen, B.-H., Improving the Surface Properties of CeO_2 by Dissolution of Ce^{3+} to Enhance the Performance for Catalytic Wet Air Oxidation of Phenol, *Ind. Eng. Chem. Res.* 56 (2017), 9090-9097.<http://doi.org/10.1021/acs.iecr.7b02121>.
- [21] Wang, J., Wang, Z., Huang, B., Ma, Y., Liu, Y., Qin, X., Zhang, X., Dai, Y., Oxygen Vacancy Induced Band-Gap Narrowing and Enhanced Visible Light Photocatalytic Activity of ZnO , *ACS Appl. Mater. Interfaces* 4 (2012), 4024-4030.<http://doi.org/10.1021/am300835p>.
- [22] Perdew, J. P., Burke, K., Ernzerhof, M. J. P. r. l., Generalized gradient approximation made simple, *Phys. Rev. Lett.* 77 (1996), 3865-11996
- [23] Kresse, G., Furthmüller, J. J. P. r. B., Efficient iterative schemes for ab initio total-energy calculations using a plane-wave basis set, *Phys. Rev. B* 54 (1996), 11169

- [24] Cheng, J., Huang, S., Li, Y., Wang, T. Q., Xie, L. L., Lu, X. C., RE (La, Nd and Yb) doped CeO₂ abrasive particles for chemical mechanical polishing of dielectric materials: Experimental and computational analysis, *App. Surf. Sci.* 506 (2020).<http://doi.org/10.1016/j.apsusc.2019.144668>.
- [25] Kresse, G., Joubert, D. J. P. r. b., From ultrasoft pseudopotentials to the projector augmented-wave method, *Phys. Rev. B* 59 (1999), 1758–1775
- [26] Murgida, G. E., Ferrari, V., Ganduglia-Pirovano, M. V., Llois, A. M., Ordering of oxygen vacancies and excess charge localization in bulk ceria: ADFT+Ustudy, *Phys. Rev. B* 90 (2014).<http://doi.org/10.1103/PhysRevB.90.115120>.
- [27] Skorodumova, N. V., Simak, S. I., Lundqvist, B. I., Abrikosov, I. A., Johansson, B., Quantum Origin of the Oxygen Storage Capability of Ceria, *Phys. Rev. Lett.* 89 (2002).<http://doi.org/10.1103/PhysRevLett.89.166601>.
- [28] Dastpak, M., Farahmandjou, M., Firoozabadi, T. P., Synthesis and Preparation of Magnetic Fe-Doped CeO₂ Nanoparticles Prepared by Simple Sol-Gel Method, *Journal of Superconductivity and Novel Magnetism* 29 (2016), 2925-2929.<http://doi.org/10.1007/s10948-016-3639-3>.
- [29] Hojo, H., Mizoguchi, T., Ohta, H., Findlay, S. D., Shibata, N., Yamamoto, T., Ikuhara, Y., Atomic Structure of a CeO₂ Grain Boundary: The Role of Oxygen Vacancies, *Nano Lett.* 10 (2010), 4668-4672.<http://doi.org/10.1021/nl1029336>.
- [30] Pang, D., Li, W., Zhang, N., He, H., Mao, S., Chen, Y., Cao, L., Li, C., Li, A., Han, X., Direct observation of oxygen vacancy formation and migration over ceria surface by in situ environmental transmission electron microscopy, *J. Rare Earths* 42 (2024), 676-682.<http://doi.org/10.1016/j.jre.2023.03.010>.
- [31] Finocchiaro, G., Ju, X., Mezghrani, B., Berret, J. F., Cerium oxide catalyzed disproportionation of hydrogen peroxide: a closer look at the reaction intermediate, *Chem. Eur. J* 30 (2024),
- [32] Esmailpour, A. A., Moradi, S., Yun, J., Scott, J., Amal, R., Promoting surface oxygen vacancies on ceria via light pretreatment to enhance catalytic ozonation, *Catal. Sci. Technol.* 9 (2019), 5979-5990.<http://doi.org/10.1039/c9cy01450k>.
- [33] Ma, J. H., Xu, N., Hu, J. R., Luo, Y. X., Lin, Y., Pu, Y. P., Doping strategy on properties and chemical mechanical polishing performance of CeO₂ Abrasives: A DFT assisted experimental study, *App. Surf. Sci.* 623 (2023).<http://doi.org/10.1016/j.apsusc.2023.156997>.
- [34] Jiang, F., Wang, S., Liu, B., Liu, J., Wang, L., Xiao, Y., Xu, Y., Liu, X., Insights into the Influence of CeO₂ Crystal Facet on CO₂ Hydrogenation to Methanol over Pd/CeO₂ Catalysts, *ACS Catalysis* 10 (2020), 11493-11509.<http://doi.org/10.1021/acscatal.0c03324>.
- [35] Li, X., Song, J., Liu, Y., Zeng, H., Controlling oxygen vacancies and properties of ZnO, *Curr. Appl Phys.* 14 (2014), 521-527.<http://doi.org/10.1016/j.cap.2014.01.007>.
- [36] Xu, N., Luo, Y., Ma, J., Lin, Y., Zhu, X., Pu, Y., Enhancement mechanism of Y-doped Ce_{1-x}Y_xO₂ for photocatalytic-assisted chemical-mechanical polishing, *Mater. Today Commun.* 38 (2024).<http://doi.org/10.1016/j.mtcomm.2023.107791>.
- [37] Phanichphant, S., Nakaruk, A., Channei, D., Photocatalytic activity of the binary composite CeO₂/SiO₂ for degradation of dye, *App. Surf. Sci.* 387 (2016), 214-

220.<http://doi.org/10.1016/j.apsusc.2016.06.072>.

[38] Mou, Q., Guo, Z., Chai, Y., Liu, B., Liu, C., Visible light assisted production of methanol from CO₂ using CdS@CeO₂ heterojunction, *Journal of Photochemistry and Photobiology B: Biology* 219 (2021).<http://doi.org/10.1016/j.jphotobiol.2021.112205>.

[39] Ansari, S. A., Khan, M. M., Ansari, M. O., Kalathil, S., Lee, J., Cho, M. H., Band gap engineering of CeO₂ nanostructure using an electrochemically active biofilm for visible light applications, *RSC Adv.* 4 (2014), 16782-16791.<http://doi.org/10.1039/c4ra00861h>.

[40] Schmitt, R., Nenning, A., Kraynis, O., Korobko, R., Frenkel, A. I., Lubomirsky, I., Haile, S. M., Rupp, J. L. M., A review of defect structure and chemistry in ceria and its solid solutions, *Chem. Soc. Rev.* 49 (2020), 554-592.<http://doi.org/10.1039/c9cs00588a>.

[41] An, X. D., Wang, J. L., Tang, X., Chen, W. L., Guan, W. K., Liu, C. Y., Peng, D. J., Experimental study and DFT plus U calculations on the impact of Rare-Earth ion (La³⁺, Sm³⁺, Y³⁺, Yb³⁺) doped CeO₂ Core-Shell abrasives on polishing performance, *App. Surf. Sci.* 676 (2024).<http://doi.org/10.1016/j.apsusc.2024.161028>.

[42] Choudhury, B., Chetri, P., Choudhury, A., Annealing temperature and oxygen-vacancy-dependent variation of lattice strain, band gap and luminescence properties of CeO₂ nanoparticles, *J. Exp. Nanosci.* 10 (2013), 103-114.<http://doi.org/10.1080/17458080.2013.801566>.

[43] Xu, L., Liu, P., Lei, H., Park, K., Kim, E., Cho, Y., Lee, J., Park, S., Kim, T., Auxiliary mechanism of in-situ micro-nano bubbles in oxide chemical mechanical polishing, *Precis. Eng.* 74 (2022), 20-35.<http://doi.org/10.1016/j.precisioneng.2021.11.005>.

[44] Xu, G. H., Zhang, Z. Y., Meng, F. N., Liu, L., Liu, D. D., Shi, C. J., Cui, X. X., Wang, J. M., Wen, W., Atomic-scale surface of fused silica induced by chemical mechanical polishing with controlled size spherical ceria abrasives, *J. Manuf. Processes* 85 (2023), 783-792.<http://doi.org/10.1016/j.jmapro.2022.12.008>.